AGU PUBLICATIONS

JGR

Journal of Geophysical Research: Space Physics

RESEARCH ARTICLE
10.1002/2017JA024631

Key Points:
- The heliospheric magnetic field (HMF) is often twisted or inverted back on itself
- Inverted HMF accounts for nearly 20% of in-ecliptic, 1 AU solar wind observations
- If not accounted for, inverted HMF can lead to an overestimate of the total open solar flux

Correspondence to:
M. J. Owens,
m.j.owens@reading.ac.uk

Citation:
Owens, M. J., Lockwood, M., Riley, P., & Linker, J. (2017). Sunward strahl: A method to unambiguously determine open solar flux from in situ spacecraft measurements using suprathermal electron data. *Journal of Geophysical Research: Space Physics*, *122*. https://doi.org/10.1002/2017JA024631

Received 1 AUG 2017
Accepted 5 NOV 2017
Accepted article online 9 NOV 2017

Sunward Strahl: A Method to Unambiguously Determine Open Solar Flux from In Situ Spacecraft Measurements Using Suprathermal Electron Data

M. J. Owens[1], M. Lockwood[1], P. Riley[2], and J. Linker[2]

[1]Space and Atmospheric Electricity Group, Department of Meteorology, University of Reading, Reading, UK, [2]Predictive Science Inc., San Diego, CA, USA

Abstract A fraction of the magnetic flux which threads the photosphere reaches sufficient coronal altitude to be dragged out by the solar wind and form the heliospheric magnetic field (HMF). Directly measuring this "open solar flux" (OSF) component, however, is difficult. While OSF can be extrapolated from photospheric magnetic field measurements, the most direct method is from in situ spacecraft measurements of the HMF. The difficultly is unambiguously distinguishing between HMF which connects directly back to the Sun (the OSF) and that which is locally distorted by waves, turbulence, and near-Sun reconnection. Suitable temporal filtering of the data can remove such "noise," but the level of filtering cannot be known a priori and varies with solar cycle, solar wind types, etc. Here we use the suprathermal electron beam, or "strahl," to distinguish between different HMF topologies. As strahl moves antisunward on global scales, times when strahl is observed to be moving sunward indicate that the HMF is locally inverted. By subtracting the inverted HMF, we compute the OSF without need for arbitrary filtering of the data. We find that the OSF obtained in this manner is slightly larger than the proposed "kinematic correction" based on observed solar wind velocity structure, though in general agreement. Our new OSF estimate agrees with methods based wholly on HMF data, if the data are first used to compute approximately 1 day averages during solar minimum and approximately 3 day averages during solar maximum, stressing the point that the filter method is unreliable because the required characteristics vary.

1. Introduction

The majority of the magnetic flux which threads the photosphere forms closed magnetic loops in the low corona that do not reach sufficient altitude to be dragged out by the solar wind and so do not, ultimately, contribute to the heliospheric magnetic field (HMF; Owens & Forsyth, 2013). It is therefore useful to define a "source surface" at the coronal altitude at which the HMF is effectively created. (Note that this need not be, and generally is not, the same height as the Alfvén surface where the solar wind flow first becomes super Alfvénic.) The total unsigned magnetic flux threading this hypothetical source surface is referred to as the "open solar flux" (OSF; e.g., Wang & Sheeley, 1995). At sunspot maximum, OSF is about 4% of the total flux threading the photosphere, but at sunspot minimum this rises to about 40% (Arge et al., 2002).

There are two principal means by which the OSF can be estimated. The first is by extrapolation of the photospheric magnetic field observations. While such measurements are currently only performed from Earth (or from near-Earth space), solar rotation allows a complete synoptic map of the photospheric magnetic field to be constructed every Carrington rotation (i.e., approximately every 27 days), though the polar fields remain poorly observed. These "magnetograms" can be extrapolated out through the corona to a source surface, typically assumed to be a sphere at 2.5 solar radii, where the OSF is estimated by integrating the unsigned radial flux. Coronal extrapolation is commonly performed using the potential field source surface approximation (Schatten, 1971; Wang et al., 2005). Moving the location of the source surface further/closer to the Sun will result in less/more OSF, respectively. Matching the modeled and observed coronal hole area can be used as a weak constraint on the source surface height (e.g., Linker et al., 2017; Stevens et al., 2012).

The second method of OSF estimation uses in situ magnetic field measurements from heliospheric spacecraft, most commonly from near-Earth space. While such single-point measurements are inherently local, longitudinal structure in the HMF can be accommodated by considering 27 day (i.e., one Carrington rotation) intervals and assuming a quasi-steady state, corotating structure to the HMF. Latitudinal structure can be

accommodated because, as *Ulysses* observed, to a high level of approximation there is very little variation in the strength of the radial magnetic field component (B_R) with latitude, once B_R is corrected for the inverse-square fall off with distance (r) (Balogh et al., 1995; Smith & Balogh, 1995). This result is to be expected because close to the Sun, where the plasma beta is low, solar wind flows will be slightly nonradial until the tangential pressure, and hence, the radial magnetic field strength is rendered uniform (Suess & Smith, 1996). This effect was initially found using averages of B_R over toward/away HMF sectors. The problem with this is that subjective decisions have to be made about which reversals in B_R are genuine sector boundaries (i.e., that map back to polarity inversions at the source surface) and which are the result of more local effects. However, Lockwood et al. (2004) used the perihelion ("fast latitude scan") passes of Ulysses to show that the latitudinal independence also applied to the modulus, $|B_R|$, taken over fixed and shorter intervals (such as 1 h). Thus, single-point measurements of $|B_R|$ at a heliocentric distance r can, in principle, be used to compute the total (unsigned) heliospheric flux threading the heliocentric sphere of radius r, $\phi_r = 4\pi\ r^2 < |B_R| >$. The (often implicit) assumption is then generally made that ϕ_r = OSF, which is discussed further below. The OSF determined by photospheric extrapolation is smaller than $\phi_{r=1\mathrm{AU}}$ by around 40% (e.g., Linker et al., 2017; Stevens et al., 2012).

In practice, however, there are a number of complications. At a general heliocentric distance r, located beyond the source surface, there are essentially two contributions to $|B_R|$: (1) magnetic flux which threads both the source surface and the heliocentric sphere of radius r in the same direction (either Toward "T" or Away "A" from the Sun) and (2) flux made up of field lines that are initially part of category (1) but then bend back to cut the surface at r one or more times: for a given T or A source field line this would give an additional $2n$ crossings of the surface at r (n in the T direction and n in the A direction) where n is an integer. There is also flux that threads the source surface, but not yet the surface at r, in the form of newly emerging closed loops and also there is flux which has been completely disconnected from the Sun but still threads the surface at r; however, flux of both these topologies would soon advect out beyond r and so are short lived. Contribution (1) is the OSF, which we would like to measure. Contribution (2) is flux that is locally distorted or inverted, as shown in Figure 1, which can result from waves, turbulence, solar wind stream sheer, near-Sun reconnection, draping around CMEs, etc., and has been termed the "excess flux" (Lockwood et al., 2009a, 2009b). As the Parker spiral HMF becomes increasingly inclined to the radial direction with increasing r, contribution (2) increases with r, and thus, ϕ_r increases with r (Lockwood et al., 2009b; Owens et al., 2008). As B_R contribution (2) is fluctuating and generally bipolar in nature, it can be subtracted by taking a long-enough time average before the modulus of B_R is computed. Increasing time averaging will reduce $|B_R|$ and hence the estimate of ϕ_r (Lockwood, Owens, & Rouillard, 2009a). The balance, of course, is that B_R from genuine OSF in the vicinity of the heliospheric current sheet (HCS) will also be increasingly canceled out with increasing time averaging (to the extreme that a 27 day average of in-ecliptic data will result in an almost zero OSF estimate). While there must exist a time averaging that results in ϕ_r = OSF, it cannot be known a priori and need not be constant, potentially changing with the solar cycle, solar wind types, heliospheric location, etc. (Of course, if the magnetic sector structure at the source surface is somehow known a priori, $< B_R >$ can be computed purely within magnetic sectors which will remove contribution (2) without any cancellation of genuine OSF. In general, however, this is not possible.) Computing the radial component of the ideal Parker spiral magnetic field, as opposed to the radial component of the total field (Erdős & Balogh, 2012, 2014) greatly reduces this r dependence on ϕ_r. Nevertheless, as is demonstrated later in this paper, the time resolution of the data still strongly influences the resulting estimate of ϕ_r and this choice remains arbitrary.

Here we seek to use additional information in the estimation of OSF from in-situ spacecraft observations. Suprathermal electrons carry heat flux from Sun and thus always move anti-sunward at the global scale (Feldman et al., 1975; Rosenbauer et al., 1977), providing a means to infer the polarity of HMF field lines at the source surface, not just the local orientation at the spacecraft (see Figure 1). When the suprathermal electron beam (or "strahl") is directed sunward, the HMF must locally be inverted. Long-duration HMF inversions were first identified close to the HCS (Crooker et al., 1996, 2004; Kahler et al., 1996; Kahler & Lin, 1994), though inversions within unipolar regions have also been observed (Balogh et al., 1999; Owens et al., 2013). In this study we use sunward strahl as a direct method to identify local HMF inversions, quantify the flux they contain, and so deduce the true OSF.

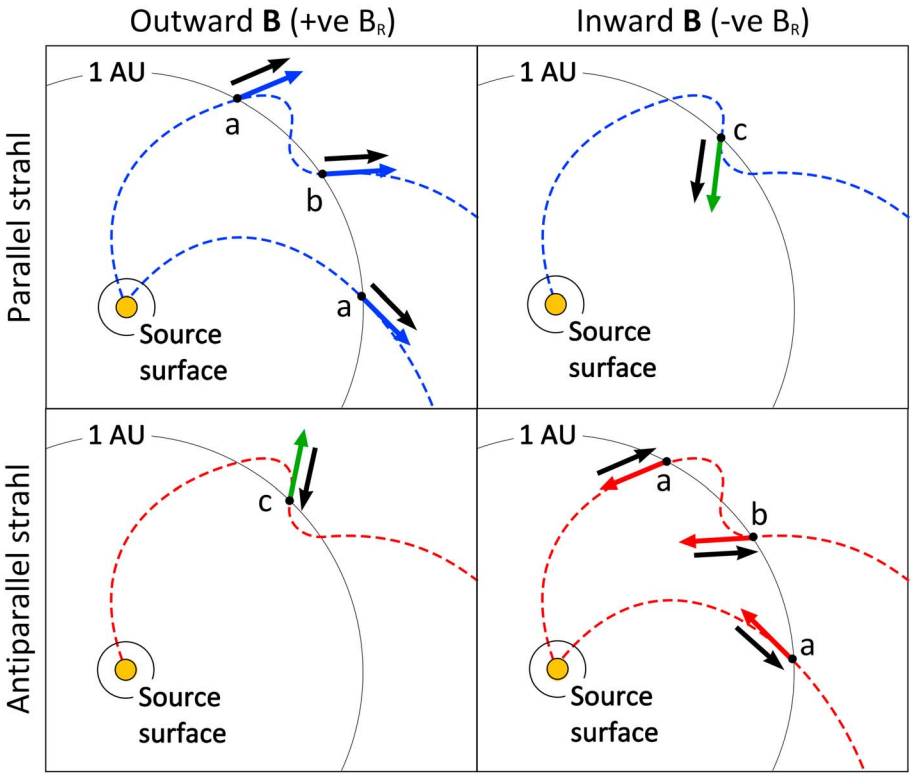

Figure 1. A schematic of the magnetic flux topologies which contribute to heliospheric flux at 1 AU. The ecliptic plane is shown. Colored arrows show the observed (local) magnetic field direction, while black arrows show the observed suprathermal electron strahl direction. Right/left columns show instances in which in situ spacecraft observations detect inward/outward polarity magnetic flux. Top/bottom row shows instances in which the strahl is parallel/antiparallel to the magnetic field. Dashed lines show potential global topologies that can be inferred from combining magnetic field and strahl information. Points labeled a have a direct magnetic connection between the point of observation and the Sun. These cannot be distinguished from b, HMF which intersects the 1 AU sphere at two further locations. Finally, c is locally inverted HMF exhibiting sunward strahl. Note that flux threading the points labeled a belongs to category (1) described in the text, whereas that at points labeled b and c contributes to category (2).

2. Data and Methods

In this study, we use the near-continuous magnetic field, plasma, and suprathermal electron data from the ACE spacecraft (McComas et al., 1998; Smith et al., 1998). While we are primarily interested in macroscale structures (i.e., approximately hourly variations in the near-Earth solar wind), averaging suprathermal electron pitch angle distributions can produce misleading results (e.g., averaging across a HMF polarity inversion could result in equal parallel and antiparallel strahl and thus the incorrect conclusion that the interval contains counterstreaming electrons and hence closed flux (Gosling et al., 1987)). For this reason, we determine HMF topology from the 64 s (i.e., spin-averaged) data. We use the entirety of the 1998–2011 available data.

The first step in determining topology is to determine the strahl direction. A number of techniques exist for fitting the suprathermal electron pitch angle distribution (Anderson et al., 2008, 2012; Hammond et al., 1996), enabling estimates of the halo, core, and strahl characteristics. Here, however, we are only interested in determining the strahl direction(s) relative to the magnetic field. Hence, we employ the simple algorithm of Owens et al. (2013), which can be readily applied to the entire ACE data set and produces very similar results to the distribution fitting methods. The mean 272 eV electron flux in the three pitch angle bins centered on 90° pitch angle (i.e., perpendicular to the magnetic field direction) is used to compute the background flux. In the absence of 90° pitch angle depletion (Gosling et al., 2001), this property is approximately equal to the "halo" population (Pilipp et al., 1987; Tao et al., 2016). The background flux is compared with the mean flux in the three most field-aligned pitch-angle bins (i.e., parallel to the magnetic field) and the mean flux in the three most antiparallel bins. If the parallel and/or antiparallel flux exceeds the background level by some threshold, a parallel and/or antiparallel strahl is determined to exist. Using other definitions of the strahl (e.g.,

the maximum, rather than mean, flux in the three pitch angle bins) will change the strahl strength but does not significantly effect strahl occurrence and hence the results presented here. In order to study specific topologies in detail, Owens et al. (2013) used a fairly strict definition of a strahl, requiring double the background flux. Here the aim is to minimize undetermined periods, which accounted for approximately 50% of the total data in Owens et al. (2013). Thus, we require parallel or antiparallel electron flux to be 30% above the background to identify strahl. In order to then avoid an overclassification of counterstreaming electron (CSE) intervals, we further require CSE to have parallel and antiparallel electron flux within 30% of each other. Directly comparing parallel and antiparallel strahl fluxes reduces the chance that a 90° pitch angle depletion (Gosling et al., 2001), which results in a low background flux estimate, is subsequently misidentified as CSE. Similarly, it reduces misinterpretation of electron reflection at Earth's bow shock (Wang et al., 2015) as CSE, as the reflected electron beam is likely to be broader in pitch angle space and lower in flux than the true strahl. This similar strahl intensity requirement could, however, potentially result in an underestimate of the occurrence of CSE as a result of true close heliospheric flux, but given closed flux contributes to OSF in the same manner as uninverted HMF, this is deemed acceptable.

Figure 1 illustrates how the magnetic field and suprathermal electron data are then combined to determine the global topology of the HMF from local measurements. When the magnetic field is outward (i.e., positive B_R) and the strahl is parallel, the field in uninverted, as shown at point a, and the local field orientation is the same as that of the field line at source surface (here termed the "global orientation"). Similarly, if the field is inward (i.e., negative B_R) and the strahl is antiparallel, it also suggests that the field is uninverted. However, it is not possible to distinguish between in-situ measurements made at point a, where the field has a direct connection between the point of measurement at 1 AU and the Sun, and those made at point b, where the field intersects the 1 AU sphere at two more locations. Finally, for this topology of field line there will be points like c, where the strahl reveals that the HMF is locally inverted with respect to the global polarity. As sketched, the field at point c is approximately orthogonal to the nominal Parker spiral direction, producing a small radial magnetic field (B_R) component, but in reality this need not be the case (Crooker et al., 2004) and the field at c could be well aligned with the expected Parker spiral direction, yet the strahl flowing back toward the Sun ("folded flux") (Owens et al., 2013). Not shown in Figure 1 are loops which close in the heliosphere at some distance beyond 1 AU. This topology can be identified by the presence of counterstreaming electrons (CSE), as strahl are generated both parallel and antiparallel to the magnetic field owing to solar connections at both magnetic foot points (Gosling et al., 1987). Such flux is nevertheless "open" insofar that it threads the source surface and contributes to the total heliospheric flux content (Owens & Crooker, 2006, 2007).

Figure 2 shows the results of applying this analysis to 2 weeks of data from October 2008. There is nothing particularly remarkable about this interval; it contains a fairly typical high-speed stream, peaking on 3 October, followed by a heliospheric current sheet crossing on 10 October. At the time of the HCS crossing, the magnetic field switches from inward (blue) to outward (red) polarity and the strahl switches from antiparallel to parallel, as expected of ideal Parker spiral (i.e., uninverted) magnetic flux. On 8 October, however, the magnetic field has an antisunward component, but the strahl is antiparallel and thus sunward, suggesting a period of locally inverted HMF, lasting between 1 to 1.5 days. The green shaded areas show that such inversions are fairly common, though this is the longest duration of such an interval in the plotted interval. Note that while all analysis is performed on 64 s data, for the purposes of plotting 1 h means are shown. Thus an interval is highlighted as, for example, inverted, if that is the dominant polarity for that hour.

3. Occurrence and Properties of Sunward Strahl

This HMF topology algorithm was applied to the entire 1998–2011 interval of 64 s ACE data, comprising approximately 7 million data points. First, the magnetic field data are considered in isolation. There are 7,412 datagaps (0.11% of total). Of the remaining data, 49.31% are positive (or outward) B_R, while 50.69% are negative (or inward) B_R. For reference, if the HMF data are instead considered in terms of angle to the ideal Parker spiral computed form the solar wind velocity, 49.53% (50.36%) of the available data are outward (inward) polarity. Considering the electron pitch angle data in isolation, 43.13% are parallel strahl, while 42.55% are antiparallel. Counterstreaming electrons account for 4.18% of the data, while the remaining

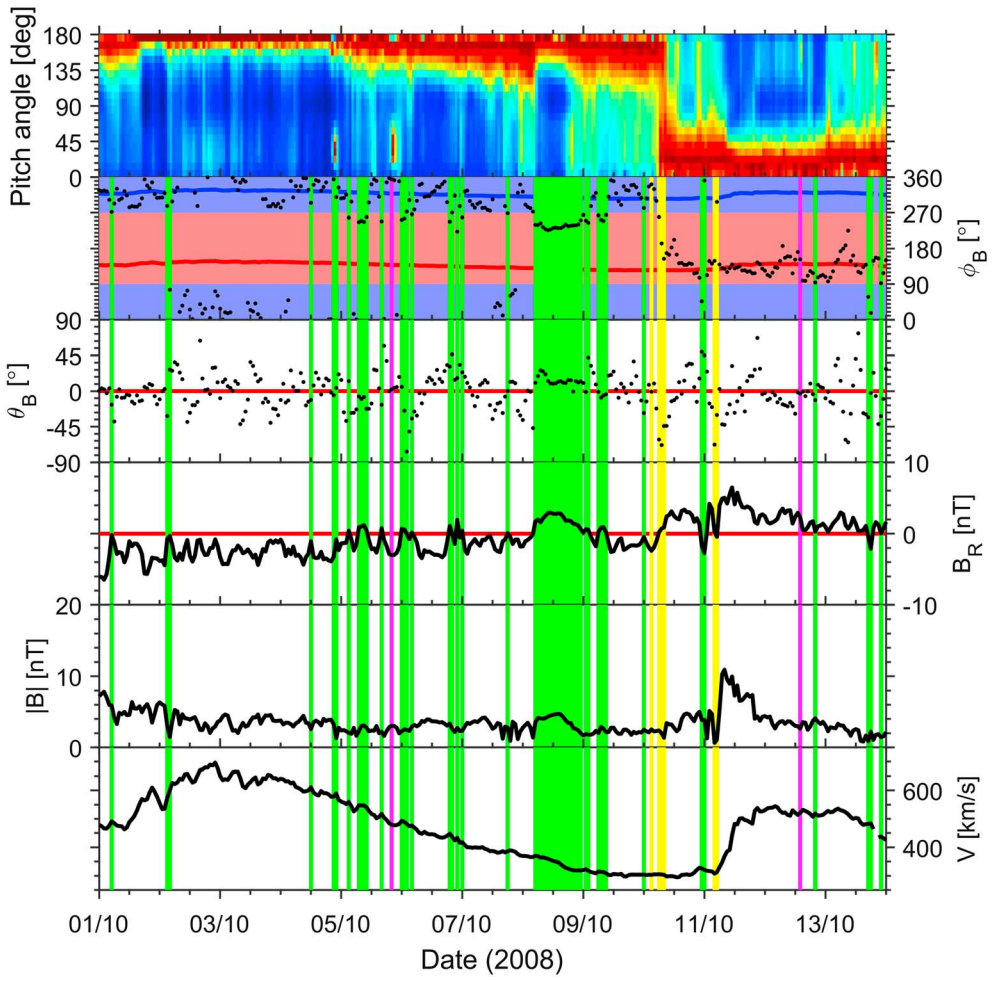

Figure 2. ACE observations from October 2008. Panels from top to bottom show the suprathermal electron pitch angle distribution (normalized to the maximum and minimum flux at each time step); φ_B, the in-ecliptic magnetic field angle in GSE coordinates; θ_B, the out-of-ecliptic angle in GSE coordinates; B_R, the radial magnetic field component (i.e., $-B_X$ in GSE coordinates); $|B|$, the magnetic field intensity; and V, the solar wind speed. In the φ_B panel, red/blue lines show the ideal Parker spiral direction for outward/inward polarity HMF. Pink/light blue shaded regions show HMF pointing away/toward the Sun. Green, pink, and yellow shaded regions show intervals of inverted HMF, counterstreaming, and undetermined HMF topology, respectively. Note that plotted data are 1 h means, whereas HMF topology is determined from 64 s data.

10.13% of the data cannot be classified, primarily as no strahl can be identified, though datagaps also contribute. Combining the HMF and electron data, 68.65% of the intervals are antisunward strahls corresponding to uninverted HMF (i.e., point a or b in Figure 1); 17.04% of the data are inverted HMF (i.e., point c in Figure 1), while 4.18% are closed HMF loops (counterstreaming strahl). The remaining 10.13% are not classified.

Figure 3 shows the correspondence between occurrence of inverted HMF and the large-scale HMF structure. While the occurrence of inverted HMF (Figure 3, top) is highly variable, there is a marked trend for it to cluster around the times of B_R polarity reversals (i.e., close to the HCS), as shown by the black lines derived in Figure 3 (bottom). Figure 4 compares the solar wind properties of antisunward strahl (i.e., uninverted HMF; black) with those of sunward strahl (i.e., inverted HMF; red). The largest difference in the two HMF populations is in the magnitude of B_R, with inverted HMF typically being associated with much weaker radial HMF. Note that the total HMF strength is very similar for inverted and uninverted HMF. Thus, inverted HMF typically makes a larger angle to the radial direction than the nominal Parker spiral at 1 AU (this is also apparent in most of the inverted HMF intervals shown in Figure 2, which are only weakly folded back toward the Sun). Both HMF populations show similar solar wind speeds, densities and α-to-proton ratios. Inverted HMF, however,

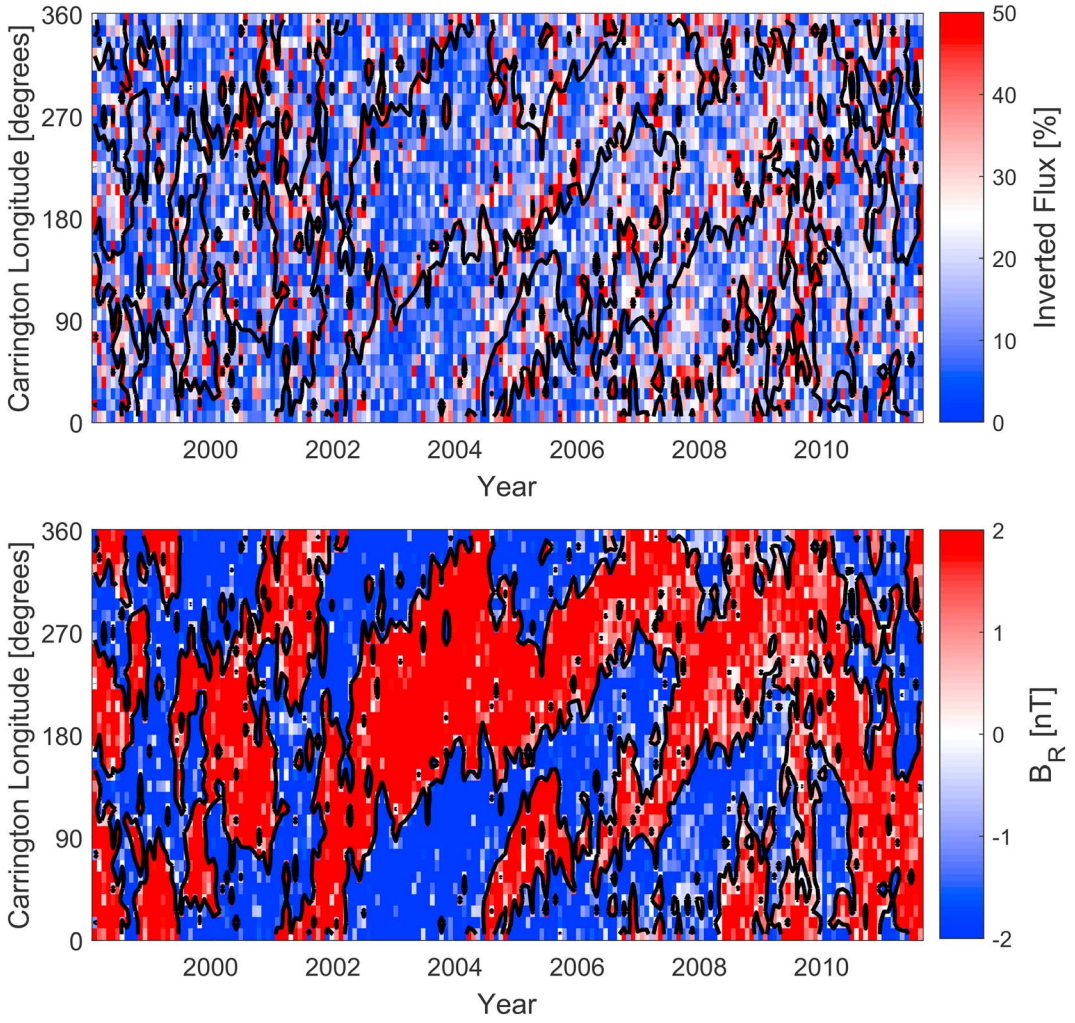

Figure 3. Carrington longitude − time maps of solar wind properties constructed from 64 s ACE data over the period 1998–2011. (top) The percentage of inverted HMF intervals in a given 10° bin (which equates to approximately 18 h averages). (bottom) The mean B_R in the same 10° bins. The black lines in both panels show the location of the HCS, defined as the transition from positive to negative B_R in adjacent 10° bins.

tends to be associated with lower proton temperatures than uninverted HMF, suggesting greater expansion and quasi-adiabatic cooling. Undetermined HMF intervals are shown in blue. They tend to occur preferentially in slower and lower magnetic field intensity solar wind, in agreement with the strahl being less obvious in slow than fast wind (Pilipp et al., 1987; Tao et al., 2016). In the next section, we compute the "best" estimate of open solar flux by assuming the proportion of inverted/uninverted flux in undetermined intervals is the same as those in which a strahl can be identified. However, to assess the uncertainty in the OSF estimate that is a result of undetermined HMF, we also consider the limiting cases of all undetermined HMF being entirely inverted or uninverted HMF. Note that while undetermined HMF accounts for 10% of the intervals, the effect on the OSF is reduced from this fraction because the strength of B_R is generally lower.

4. The Effect of Sunward Strahl on Open Solar Flux Estimates

Next, we compute the open solar flux from in situ spacecraft data using a range of methods. For all methods, we average over any longitudinal structure in HMF by considering 27.27 day (i.e., Carrington rotation) intervals. Then we extrapolate from in-ecliptic measurements to global magnetic flux assuming a latitudinal invariance of $|B_R|$.

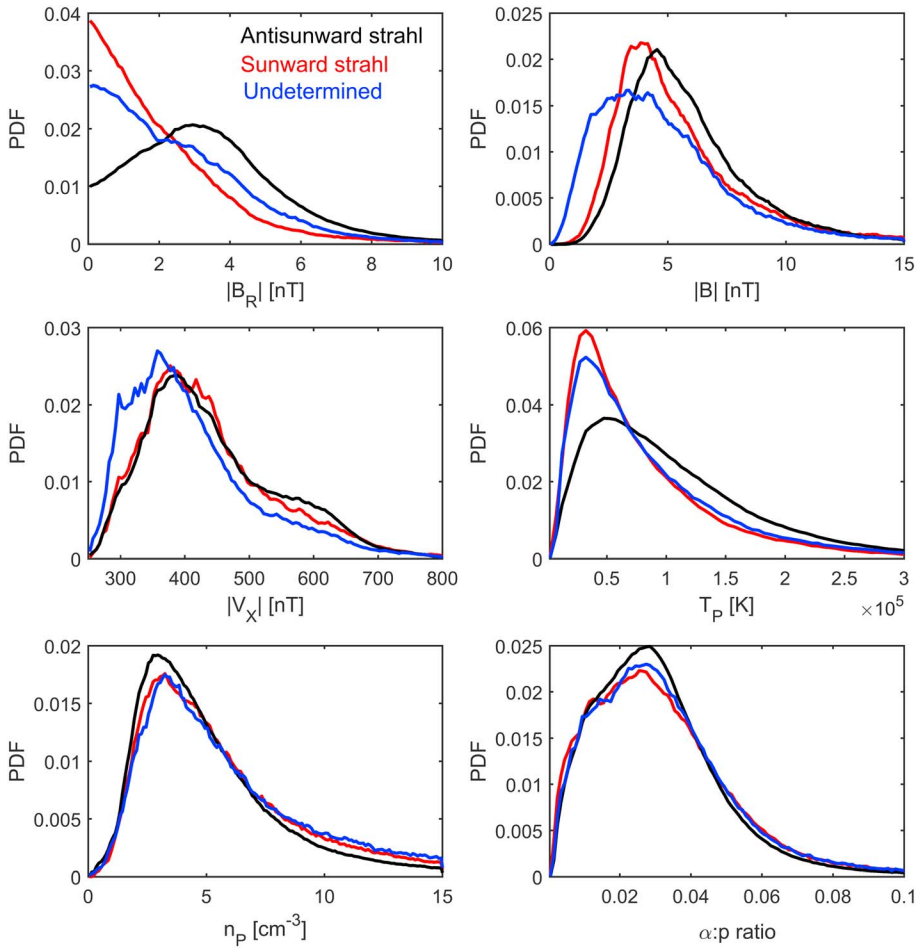

Figure 4. Probability distribution functions of solar wind parameters during periods of uninverted (black), inverted (red), and undetermined HMF (blue). From top left: the modulus of radial field, $|B_R|$; the IMF magnitude, B; the radial solar wind velocity, $|V_X|$; the proton temperature, T_P; the proton number density, n_P; and the ratio of number densities of alpha particles and protons, α:p.

The first method we consider is to compute $\Phi_{r=1\mathrm{AU}} = 4\pi r^2 < |B_R| >$ using a 27 day average of $|B_R|$ and to simply assume this is equal to the OSF. The complication, of course, is the time resolution of the data on which the modulus of B_R is first computed. Figure 5 (left) shows $\Phi_{r=1\mathrm{AU}}$ calculated using $|B_R|$ from 64 s, 1 h, 1 day, and 5 day B_R data. As highlighted by Lockwood et al. (2009a), the choice of time resolution for the initial data is arbitrary yet significantly affects the resulting OSF estimate because of the varying degree of in-out flux cancellation in each averaging interval. Figure 5 (right) shows the same effect for OSF computed using the Erdős and Balogh (2012) method, wherein the radial component of the ideal Parker spiral field, rather than the radial component of the total field, is used. For the highest time-resolution data (64 s), the Parker component method produces lower OSF estimates than $4\pi r^2|B_R|$, as it effectively filters out some of the "noise" in B_R from small-scale structures and wave activity. As the time resolution of the B_R data is reduced, however, there is increasingly smaller difference in the OSF estimates from the two methods. Of course, this is purely 1 AU data and the value of the Parker component method is that it can be readily applied to data from a range of heliocentric distances without further correction. But as seen in Figure 5, it nevertheless requires an arbitrary choice of data resolution which can have a large effect on the resulting OSF estimate; the difference in OSF computed from 64 s data and the 6 h data used in Erdős and Balogh (2012) and Erdős and Balogh (2014) is typically around 20%.

In order to avoid the need to guess at the correct time averaging interval which needs to be applied to the B_R data to give $\Phi_{r=1\mathrm{AU}}$ = OSF, we now use the suprathermal electron data to directly quantify the magnetic flux contained in the nonsource surface component (2) of $\Phi_{r=1\mathrm{AU}}$. This is the magnetic flux contained in sunward

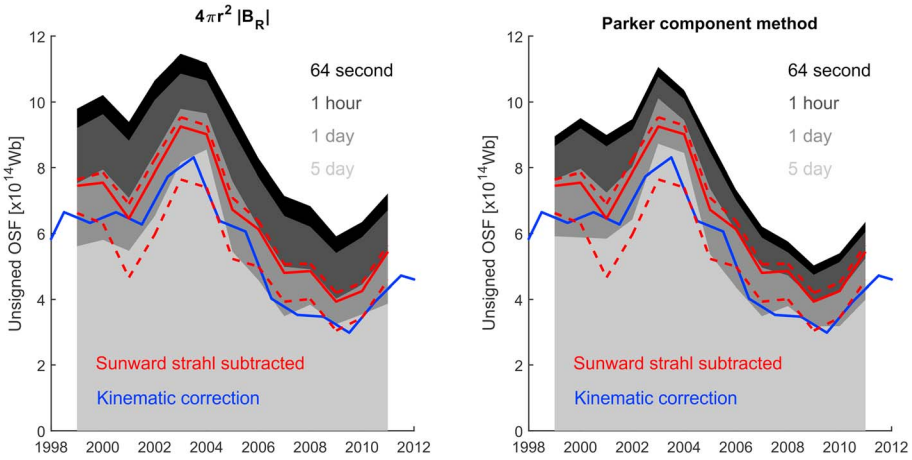

Figure 5. Unsigned open solar flux (OSF) estimates from ACE data using a range of methods. (left) The different grey-shaded regions show OSF estimated from $4\pi r^2|B_R|$ using ACE data at different initial time resolutions. (right) shows the same data analyzed using the Parker component method of Erdős and Balogh (2012). The blue line shows OSF estimates based on the kinematic-correction to $\phi_{r=1\,\mathrm{AU}}$ (Lockwood & Owens, 2009; Lockwood et al., 2009a, 2009b). Finally, the dashed and solid red lines show the upper and lower bounds and best estimate, respectively, of OSF obtained by subtracting sunward strahl from $\phi_{r=1\,\mathrm{AU}}$. All sequences have been annually averaged.

strahl intervals (topology *c*), $\phi_c$plus the magnetic flux contained in the (unidentifiable) return HMF (topology b), ϕ_b. By conservation of magnetic flux, $\phi_c = \phi_b$ and thus the total OSF, ϕ_{OSF}, is given by

$$\begin{aligned}\phi_{\mathrm{OSF}} &= \phi_{r=1\mathrm{AU}} - [\phi_c + \phi_b] \\ &= \phi_{r=1\mathrm{AU}} - 2\phi_c\end{aligned}$$

In order to estimate these quantities, the following approach is adopted. For each Carrington rotation, we determine the average $|B_R|$ for antisunward strahl (uninverted HMF), sunward strahl (inverted HMF), closed, unclassified and all HMF types, referred to as $<|B_R|>_{\mathrm{AS}}$, $<|B_R|>_{\mathrm{SS}}$, $<|B_R|>_{\mathrm{CL}}$, $<|B_R|>_{\mathrm{U}}$, and $<|B_R|>_{\mathrm{ALL}}$, respectively, as well as the number of 64 s intervals of each type, N_{ASI}, N_{SS}, N_{CL}, N_{U}, and N_{ALL}. Thus, for a given Carrington rotation, the total magnetic flux threading the 1 AU sphere ($\phi_{r=1\,\mathrm{AU}}$) is given by

$$\begin{aligned}\phi_{r=1\mathrm{AU}} &= 4\pi\, r^2 <|B_R|>_{\mathrm{ALL}} \\ &= \frac{4\pi\, r^2}{N_{\mathrm{ALL}}}\left[N_{AS} <|B_R|>_{AS} + N_{SS} <|B_R|>_{SS} + N_{CL} <|B_R|>_{CL} + N_U <|B_R|>_U\right]\end{aligned}$$

This is, of course, identical to $4\pi R^2|B_R|$ using the modulus of B_R computed on 64 s data. The next step is to subtract the contribution to $\phi_{r=1\,\mathrm{AU}}$ which does not connect directly to the source surface (i.e., intervals equivalent to points b and c in Figure 1). This contribution is given by (the r = 1 AU subscript is dropped, for convenience):

$$\phi_c = 4\pi\, r^2\left[N_{SS}\langle|B_R|\rangle_{SS} + \frac{N_{SS}}{N_{\mathrm{ALL}}} N_U\langle|B_R|\rangle_U\right]$$

where the second term arises from assuming that a fraction of the unclassified intervals which are inverted flux are in the same proportion as the rest of the Carrington rotation. We also consider the limiting cases that all the unidentified HMF is either inverted or uninverted HMF, which results in lower and upper bounds on the OSF estimate, respectively:

$$\begin{aligned}\phi_c{}^{\mathrm{LOW}} &= 4\pi\, R^2\left[N_{SS}\langle|B_R|\rangle_{SS} + N_U\langle|B_R|\rangle_U\right] \\ \phi_c{}^{\mathrm{HIGH}} &= 4\pi\, R^2 N_{SS}\langle|B_R|\rangle_{SS}\end{aligned}$$

The red lines in Figure 5 show ϕ_{OSF} estimated by this method. The solid red line shows the best estimate, from assuming the undetermined HMF contains inverted and uninverted HMF in the same proportions as the rest of the data set. The dashed lines show the OSF resulting from the upper and lower limits to the inverted flux (giving a lower and upper limits to the OSF).

The blue line shows the kinematic correction to the $4\pi r^2|B_R|$ OSF estimate, computed using the observed solar wind speed variations (Lockwood & Owens, 2009; Lockwood et al., 2009a, 2009b). In this correction, the observed temporal variation of the radial solar wind velocity is interpreted as longitudinal structure. The frozen-in flux theorem and the observed field tangential to the velocity shear are used to compute the degree to which tangential field was converted to radial field during the passage of the solar wind from the source surface to the spacecraft. Over the whole OMNI data set (1964–2014), the kinematically corrected OSF was estimated to be roughly equivalent to $4\pi R^2|B_R|$ based on 1 day B_R data. Over this limited time period, however, it is somewhere between 1 day and 5 day B_R.

The kinematic correction to $4\pi R^2|B_R|$ agrees with the sunward strahl subtraction method within uncertainties, though the kinematic correction generally tends to be lower. The OSF estimated using only the 1 AU magnetic field observations (i.e., uncorrected $4\pi R^2|B_R|$ and the Parker component method) agrees with these two "corrected" methods if magnetic field data is first averaged to between 1 and 3 day resolution, though the required time averaging appears to be variable over the solar cycle.

5. Discussion and Conclusions

We have surveyed local heliospheric magnetic field (HMF) inversions at $r = 1$ AU, identified by a characteristic "sunward strahl" suprathermal electron signatures. HMF inversions account for approximately 20% of the 64 s ACE data over the interval 1998–2011. They are found throughout the solar cycle and in a wide range of solar wind conditions, though there is a weak trend for them to cluster close to the location of the heliospheric current sheet. Magnetic field strength within sunward strahl is comparable to that of the rest of the solar wind. The radial component of the magnetic field (B_R), however, is significantly weaker within sunward strahl than in the solar wind in general. This suggests that the bulk of the HMF inversions are only just folded back toward the Sun.

Using this global HMF topology information, we calculate the open solar flux without any arbitrary choice of time resolution or additional correction, and without subjective decisions about which radial field reversals are sector boundaries that map back to the source surface. It is important to use high time resolution data for this analysis, as if the duration of inverted flux intervals is significantly shorter than the cadence of observations, the HMF topology could be incorrectly determined. Our "sunward strahl subtracted" OSF estimate is in rough agreement (within 10%) with the kinematically corrected OSF estimate (Lockwood & Owens, 2009; Lockwood et al., 2009a, 2009b), which instead uses solar wind speed data to empirically remove the effect of HMF inversions. There is some evidence, however, that the kinematic correction is slightly too strong during this period. We find agreement of the sunward strahl subtracted OSF with both a simple $4\pi R^2|B_R|$ calculation of OSF and the Parker-spiral method of Erdős and Balogh (2012), as long as the data are first averaged to somewhere between 1 and 3 day resolution. The required time averaging to effectively remove HMF inversions varies over the solar cycle, with it being closer to 1 day near solar minimum and closer to 3 days at solar maximum. We point out that the effective time averaging varies as a result of amount of inverted HMF and thus is expected to be a function of heliospheric location, solar wind type, etc., as well as solar cycle.

This study is based on data taken in near-Earth space and so assumes that the behavior, in terms of the fraction of inverted flux at other heliographic latitudes, is the same as seen in the ecliptic plane. This is likely to be valid at sunspot maximum when the streamer belt covers all heliographic latitudes. At sunspot minimum, however, the streamer belt will be relatively narrow and behavior need not be the same within the streamer belt and in the polar coronal holes, both of which could be sampled by near-Earth interplanetary spacecraft. This will be investigated in a subsequent study.

Acknowledgments
Magnetic field, plasma and suprathermal electron data were obtained from the ACE Science Center (ASC) at http://www.srl.caltech.edu/ACE/ASC/. M. O. and M. L. are part funded by Science and Technology Facilities Council (STFC) grant ST/M000885/1. P. R. gratefully acknowledges NASA's LWS TR&T program (NNX15AF39G) for support in undertaking this study.

References

Anderson, B. R., Skoug, R. M., Steinberg, J. T., & McComas, D. J. (2008). Comparison of the width and intensity of the suprathermal electron Strahl in general solar wind and ICME solar wind. AGU Fall Meeting Abstracts A1580. https://doi.org/10.1016/j.hal.2008.08.017

Anderson, B. R., Skoug, R. M., Steinberg, J. T., & McComas, D. J. (2012). Variability of the solar wind suprathermal electron strahl. *Journal of Geophysical Research*, *117*, A04107. https://doi.org/10.1029/2011JA017269

Arge, C. N., Hildner, E., Pizzo, V. J., & Harvey, J. W. (2002). Two cycles of nonincreasing magnetic flux. *Journal of Geophysical Research*, *107*(A10), 1319. https://doi.org/10.1029/2001JA000503

Balogh, A., Forsyth, R. J., Lucek, E. A., Horbury, T. S., & Smith, E. J. (1999). Heliospheric magnetic field polarity inversions at high heliographic latitudes. *Geophysical Research Letters*, *26*(6), 631–634. https://doi.org/10.1029/1999GL900061

Balogh, A., Southwood, D. J., Forsyth, R. J., Horbury, T. S., Smith, E. J., & Tsurutani, B. T. (1995). The heliospheric magnetic field over the south polar region of the Sun. *Science*, *268*(5213), 1007–1010. https://doi.org/10.1126/science.268.5213.1007

Crooker, N. U., Burton, M. E., Siscoe, G. L., Kahler, S. W., Gosling, J. T., & Smith, E. J. (1996). Solar wind streamer belt structure. *Journal of Geophysical Research*, *101*(A11), 24,331–24,341. https://doi.org/10.1029/96JA02412

Crooker, N. U., Kahler, S. W., Larson, D. E., & Lin, R. P. (2004). Large-scale magnetic field inversions at sector boundaries. *Journal of Geophysical Research*, *109*, A03108. https://doi.org/10.1029/2003JA010278

Erdős, G., & Balogh, A. (2012). Magnetic flux density measured in fast and slow solar wind streams. *The Astrophysical Journal*, *753*(2), 130. https://doi.org/10.1088/0004-637X/753/2/130

Erdős, G., & Balogh, A. (2014). Magnetic flux density in the heliosphere through several solar cycles. *The Astrophysical Journal*, *781*(1), 50. https://doi.org/10.1088/0004-637X/781/1/50

Feldman, W. C., Asbridge, J. R., Bame, S. J., Montgomery, M. D., & Gary, S. P. (1975). Solar wind electrons. *Journal of Geophysical Research*, *80*(31), 4181–4196. https://doi.org/10.1029/JA080i031p04181

Gosling, J. T., Baker, D. N., Bame, S. J., Feldman, W. C., & Zwickl, R. D. (1987). Bidirectional solar wind electron heat flux events. *Journal of Geophysical Research*, *92*(A8), 8519–8535. https://doi.org/10.1029/JA092iA08p08519

Gosling, J. T., Skoug, R. M., & Feldman, W. C. (2001). Solar wind electron halo depletions at 90-degree pitch angle. *Geophysical Research Letters*, *28*(22), 4155–4158. https://doi.org/10.1029/2001GL013758

Hammond, C. M., Feldman, W. C., McComas, D. J., Phillips, J. L., & Forsyth, R. J. (1996). Variation of electron-strahl width in the high-speed solar wind: ULYSSES observations. *Astronomy and Astrophysics*, *316*, 350–354.

Kahler, S., & Lin, R. P. (1994). The determination of interplanetary magnetic field polarities around sector boundaries using $E > 2$ keV electrons. *Geophysical Research Letters*, *21*(15), 1575–1578. https://doi.org/10.1029/94GL01362

Kahler, S. W., Crooker, N. U., & Gosling, J. T. (1996). The topology of intrasector reversals of the interplanetary magnetic field. *Journal of Geophysical Research*, *101*(A11), 24,373–24,382. https://doi.org/10.1029/96JA02232

Linker, J. A., Caplan, R. M., Downs, C., Riley, P., Mikic, Z., Lionello, R., … Owens, M. J. (2017). The open flux problem. *The Astrophysical Journal*, *848*(1). https://doi.org/10.3847/1538-4357/aa8a70

Lockwood, M., Forsyth, R. J., Balogh, A., & McComas, D. J. (2004). Open solar flux estimates from near-Earth measurements of the interplanetary magnetic field: Comparison of the first two perihelion passes of the Ulysses spacecraft. *Annales Geophyscae*, *22*(4), 1395–1405. https://doi.org/10.5194/angeo-22-1395-2004

Lockwood, M., & Owens, M. (2009). The accuracy of using the Ulysses result of the spatial invariance of the radial heliospheric field to compute the open solar flux. *The Astrophysical Journal*, *701*(2), 964–973. https://doi.org/10.1088/0004-637X/701/2/964

Lockwood, M., Owens, M., & Rouillard, A. P. (2009a). Excess open solar magnetic flux from satellite data: 1. Analysis of the third perihelion Ulysses pass. *Journal of Geophysical Research*, *114*, A11103. https://doi.org/10.1029/2009JA014449

Lockwood, M., Owens, M., & Rouillard, A. P. (2009b). Excess open solar magnetic flux from satellite data: 2. A survey of kinematic effects. *Journal of Geophysical Research*, *114*, A11104. https://doi.org/10.1029/2009JA014450

McComas, D. J., Bame, S. J., Barker, S. J., Feldman, W. C., Phillips, J. L., Riley, P., & Griffee, J. W. (1998). Solar wind electron proton alpha monitor (SWEPAM) for the Advanced Composition Explorer. *Space Science Reviews*, *86*(1/4), 563–612. https://doi.org/10.1023/A:1005040232597

Owens, M. J., Arge, C. N., Crooker, N. U., Schwadron, N. A., & Horbury, T. S. (2008). Estimating total heliospheric magnetic flux from single-point in situ measurements. *Journal of Geophysical Research*, *113*, A12103. https://doi.org/10.1029/2008JA013677

Owens, M. J., & Crooker, N. U. (2006). Coronal mass ejections and magnetic flux buildup in the heliosphere. *Journal of Geophysical Research*, *111*, A10104. https://doi.org/10.1029/2006JA011641

Owens, M. J., & Crooker, N. U. (2007). Reconciling the electron counterstreaming and dropout occurrence rates with the heliospheric flux budget. *Journal of Geophysical Research*, *112*, A06106. https://doi.org/10.1029/2006JA012159

Owens, M. J., Crooker, N. U., & Lockwood, M. (2013). Solar origin of heliospheric magnetic field inversions: Evidence for coronal loop opening within pseudostreamers. *Journal of Geophysical Research*, *118*(5), 1868–1879. https://doi.org/10.1002/jgra.50259

Owens, M. J., & Forsyth, R. J. (2013). The heliospheric magnetic field. *Living Reviews in Solar Physics*, *10*, 5. https://doi.org/10.12942/lrsp-2013-5

Pilipp, W. G., Muehlhaeuser, K.-H., Miggenrieder, H., Rosenbauer, H., & Schwenn, R. (1987). Variations of electron distribution functions in the solar wind. *Journal of Geophysical Research*, *92*(A2), 1103–1118. https://doi.org/10.1029/JA092iA02p01103

Rosenbauer, H., Schwenn, R., Marsch, E., Meyer, B., Miggenrieder, H., Montgomery, M. D., … Zink, S. M. (1977). A survey on initial results of the HELIOS plasma experiment. *Journal of Geophysics Zeitschrift Geophysik*, *42*, 561–580.

Schatten, K. H. (1971). Current sheet magnetic model for the solar corona. *Cosmic Electrodynamics*, *2*, 232–245.

Smith, C. W., L'Heureux, J., Ness, N. F., Acuna, M. H., Burlaga, L. F., & Scheifele, J. (1998). The ACE magnetic fields experiment. *Space Science Reviews*, *86*(1/4), 613–632. https://doi.org/10.1023/A:1005092216668

Smith, E. J., & Balogh, A. (1995). Ulysses observations of the radial magnetic field. *Geophysical Research Letters*, *22*(23), 3317–3320. https://doi.org/10.1029/95GL02826

Stevens, M. L., Linker, J. A., Riley, P., & Hughes, W. J. (2012). Underestimates of magnetic flux in coupled MHD model solar wind solutions. *Journal of Atmospheric and Solar-Terrestrial Physics*, *83*, 22–31. https://doi.org/10.1016/j.jastp.2012.02.005

Suess, S. T., & Smith, E. J. (1996). Latitudinal dependence of the radial IMF component: Coronal imprint. *Geophysical Research Letters*, *23*(22), 3267–3270. https://doi.org/10.1029/96GL02908

Tao, J., Wang, L., Zong, Q., Li, G., Salem, C. S., Wimmer-Schweingruber, R. F., … Bale, S. D. (2016). QUIET-TIME SUPRATHERMAL (~ 0.1–1.5 keV) ELECTRONS IN THE SOLAR WIND. *The Astrophysical Journal*, *820*(1), 22. https://doi.org/10.3847/0004-637X/820/1/22

Wang, X., Tu, C., Wang, L., He, J., & Marsch, E. (2015). The upstream-propagating Alfvénic fluctuations with power law spectra in the upstream region of the Earth's bow shock. *Geophysical Research Letters*, *42*(10), 3654–3661. https://doi.org/10.1002/2015GL063893

Wang, Y.-M., Lean, J., & Sheeley, N. Jr. (2005). Modeling the Sun's magnetic field and irradiance since 1713. *The Astrophysical Journal*, *625*(1), 522–538. https://doi.org/10.1086/429689

Wang, Y.-M., & Sheeley, N. R. (1995). Solar implications of *Ulysses* interplanetary field measurements. *The Astrophysical Journal Letters*, *447*(2), L143–L146. https://doi.org/10.1086/309578